ADVANCED FUNCTIONAL MATERIALS

Supporting Information

for *Adv. Funct. Mater.*, DOI 10.1002/adfm.202307998

Nondestructively Visualizing and Understanding the Mechano-Electro-chemical Origins of "Soft Short" and "Creeping" in All-Solid-State Batteries

*Daxian Cao, Kena Zhang, Wei Li, Yuxuan Zhang, Tongtai Ji, Xianhui Zhao, Ercan Cakmak, Juner Zhu, Ye Cao and Hongli Zhu**

Supplementary Materials

Nondestructively Visualizing and Understanding the Mechano-Electrochemical Origins of "Soft Short" and "Creeping" in All-solid-state Batteries

Daxian Cao[1,#], Kena Zhang[2,#], Wei Li[1], Yuxuan Zhang[3], Tongtai Ji[1], Xianhui Zhao[4], Ercan Cakmak[5], Juner Zhu[1], Ye Cao[2], Hongli Zhu[1,]*

[1]Department of Mechanical and Industrial Engineering, Northeastern University, Boston, Massachusetts 02115, USA.

[2]Department of Materials Science and Engineering, The University of Texas at Arlington, Arlington, TX, 76019, USA

[3]Neutron Scattering Division, Oak Ridge National Laboratory, Oak Ridge, Tennessee 37831, USA.

[4]Manufacturing Science Division, Oak Ridge National Laboratory, Oak Ridge, Tennessee 37831, USA.

[5]Materials Science and Technology Division, Oak Ridge National Laboratory, Oak Ridge, Tennessee 37831, USA

#: These authors contributed equally to this work.

***Correspondence:** Dr. Hongli Zhu (h.zhu@neu.edu)

This PDF file includes:

Other Supplementary Materials for this manuscript include the following:

Video S1 to S6

Supplementary Text I

Phase field modeling

The total free energy (F) of the inhomogeneous system is written as,

$$F = \int_V [f_{ch}(\xi, \rho, c_i^*) + f_{grad}(\nabla\xi, \nabla\rho) + f_{elec}(c_i^*, \varphi) + f_{elas}(e_{ij}, \xi)]dV \quad \text{(Eq. S1)}$$

where f_{ch}, f_{grad}, f_{elec}, and f_{elas} represent the local energy density from chemical, gradient, electrostatic, and elastic contribution, respectively. $c_i^* = c_i / c_0$ is a set of dimensionless concentration of species, (i.e., i = Li^+, e^-), where c_0 is the standard bulk concentration. φ is the electrostatic potential. The chemical free energy density f_{ch} is given by the summation of a local free energy density f_0 and the energy of ion mixing f_{ion}. The local free energy density is described as $f_0(\xi, \rho) = W_\xi \xi^2 (1-\xi)^2 + W_\rho \left(\rho^2 - 1\right)\rho + \frac{A}{2}\xi^2\rho^2$, in which the energy coefficients (W_ξ, W_ρ) are set to be 0.25 and 1, which represent the barrier heights of the double wells[3]. We assume The energy of ion mixing can be represented as $f_{\text{ion}} = c_0 RT \sum_i c_i^* \ln c_i^*$ in a diluted electrolyte where c_i (i = Li, Li^+ and A^-) denote the concentrations of the Li metal, cation and anion. The interfacial energy induced at the interfaces of the Li dendrite, solid electrolyte, and pores is accounted for by the gradient energy $f_{grad}(\nabla\xi, \nabla\phi) = \frac{\kappa_\xi}{2}(\nabla\xi)^2 + \frac{\kappa_\rho}{2}(\nabla\rho)^2$, where the κ_ξ and κ_ρ

are the gradient coefficients associated with Li metal surface energy and pore surface energy. The anisotropy of surface energy will eventually leads to the Li dendritic morphology which is determined by $\kappa_\xi = \kappa_0[1+\delta\cos(\omega\theta)]$, where κ_0 is related to the average Li metal surface energy and the interface width, δ and ω are the strength and mode of the anisotropy, and θ is the angle between the normal vector of the dendrite/electrolyte interface and the reference axis.

The electrostatic energy density is given by $f_{elec}(c_i,\varphi) = \sum z_i F c_i \varphi$, where z_i and F denote the charge number of the species c_i and the Faraday's constant, respectively. The elastic energy density (f_{elas}) is written as $f_{elas} = \frac{1}{2}C_{ijkl}e_{ij}e_{kl} = \frac{1}{2}C_{ijkl}(\xi,\rho)(\varepsilon_{ij}-\varepsilon_{ij}^0)\cdot(\varepsilon_{kl}-\varepsilon_{kl}^0)$, where C_{ijkl} is the stiffness tensor. ε_{ij} is the total strain and $\varepsilon_{ij}^0 = V_{ij}\xi\delta_{ij}$ is the local eigenstrain ($\varepsilon_{ij}^0 = V_{ij}\xi\delta_{ij}$) where V_{ij} is the Vegard strain coefficients obtained in previous literatures[1].

The transport of Li^+ in the cell can be described by the Nernst-Planck equation,

$$\frac{\partial c_{Li^+}}{\partial t} = \nabla\cdot\left[D_{Li^+}^{eff}\nabla c_{Li^+} + D_{Li^+}^{eff}c_{Li^+}\frac{F}{RT}\nabla\varphi\right] - K\frac{\partial\xi}{\partial t} \qquad \text{(Eq. S2)}$$

Here, $D_{Li^+}^{eff} = D_{Li^+}^{m}h(\xi) + D_{Li^+}^{e}(1-h(\xi))$ represents the diffusion coefficient of Li^+, $D_{Li^+}^{m}$ and $D_{Li^+}^{e}$ are the diffusion coefficients of Li^+ in the Li metal and the electrolyte, respectively. In the porous electrolyte, we assume that the diffusion coefficient of Li^+ at the interface between the pore and the electrolyte D_{surf}^{ρ} is four orders of magnitude higher than in electrolyte itself D_{bulk}^{e}, while it is zero

inside the pore D_{in}^{ρ}. c_{Li^+} the initial concentration of electrode. The accumulation/annihilation rate of Li^+ due to the electrochemical reaction on the surface of the anode is proportional to the phase change rate $\frac{\partial \xi}{\partial t}$ through the accumulation constant *K*.

The electrostatic potential distribution can be expressed by,

$$\nabla \cdot (\sigma^{eff} \nabla \varphi) = R \frac{\partial \xi}{\partial t} \qquad \text{(Eq. S3)}$$

Herein, $\sigma^{eff} = \sigma^m h(\xi) + \sigma^e (1 - h(\xi))$ is the effective electric conductivity, where σ^m and σ^e represent the electric conductivities of electrode and electrolyte, respectively.

The mechanical equilibrium equation is given by,

$$\nabla \cdot \left(C_{ijkl} e_{kl} \right) = 0 \qquad \text{(Eq. S4)}$$

where $C_{ijkl} = \frac{E^{eff}}{2(1+\nu)} \left(\delta_{il}\delta_{jk} + \delta_{ik}\delta_{jl} \right) + \frac{E^{eff}\nu}{(1+\nu)(1-2\nu)} \delta_{ij}\delta_{kl}$ is the stiffness tensor, e_{kl} denotes the elastic strain tensor. The elastic modulus $E^{eff} = E^m h(\xi) + E^e (1 - h(\xi))$ is contributed by the Li metal and the solid electrolyte ($E^m = E^e =$ 5 GPa). In the electrolyte, we assume that the Young's modulus of pore is the same as air pressure ($E^{\rho} = 1 \times 10^{-4}$ GPa). To better visualize the mechanical response, we use the hydrostatic pressure (P_m) and strain (ε_{vol}), which are evaluated by averaging the normal stress and strain component, i.e., $P_m = \frac{1}{3}(\sigma_{xx} + \sigma_{yy} + \sigma_{zz})$ and $\varepsilon_{vol} = \frac{1}{3}(e_{xx} + e_{yy} + e_{zz})$.

In this work, we ignore plastic deformation and assume that the Li metal and electrolyte are both treated as linear elastic materials for simplification.

Supplementary Text II

Finite element model

The finite element model includes both the cell components (cathode, SE, and lithium metal) and the holder (PTFE tube and stainless-steel bars). Material models should be carefully selected to characterize the mechanical behaviors of each component[2].

Lithium metal is typical metal material and a few groups have tested its bulk mechanical properties as a foil[3]. It deforms plastically with slight hardening under a high stress level, while creep dominates under a low stress level. In this work, the lithium metal undergoes relatively high stress compared to its yield stress, and therefore, we only consider the plastic flow with the classical von Mises yield criterion, which states that material begins to yield when the equivalent stress $\underline{\sigma}$ reaches a critical value $\underline{\sigma_Y}$. This critical value evolves with the accumulated equivalent plastic strain $\underline{\varepsilon_p}$ and describes the hardening behavior of a material. For materials with low hardening rate like lithium, the Voce hardening law

$$\underline{\sigma_Y} = \sigma_0 + (\sigma_s - \sigma_0)\left(1 - exp\ exp\left(-\beta \underline{\varepsilon_p}\right)\right), \qquad \text{(Eq. S5)}$$

is commonly used[2-3], where σ_0 (initial yield stress), σ_s (saturated yield stress), and β (hardening rate) are the material constants to be calibrated.

The cathode and SE are granular porous media; therefore, we adopted the Drucker-Prager/Cap (DPC) model, which is commonly used for geomaterials. The yield surface of DPC model has two branches, namely the shear failure (sliding) surface and consolidation surface. These two yield

surfaces characterize the two main deformation mechanisms of granular materials, the inter-granular sliding, and intra-granular consolidation, respectively. Fully calibrating this model requires a comprehensive set of tests, including uniaxial compression, Brazilian test (lateral compression), and confined compression. Zhu et al.[4] have calibrated the DPC model for NMC and graphite coatings in a liquid Li-ion cell. For SEs, a complete set of experimental data for calibration has not yet been reported. We have collected limited data in the literature[4] and estimated some material constants to calibrate the DPC model for SE.

The PTFE tube is also characterized by the von Mises plasticity model and a linear plastic hardening behavior is assumed, $\underline{\sigma_Y} = \sigma_0 + H\underline{\varepsilon_p}$, where H is the linear hardening rate. For stainless-steel bars, linear elasticity model is used since the yield stress of steel is higher than the applied pressure in this work and only elastic deformation will occur. The material constants of each component are listed in Table S3**.** The detailed description of material models and calibration process are provided in the following.

von Mises plasticity model

von Mises plasticity model states that a material begins to yield when the equivalent stress $\underline{\sigma}$ reaches a critical value $\underline{\sigma_Y}$. The equivalent stress $\underline{\sigma}$ is defined as

$$\underline{\sigma} = \sqrt{\frac{1}{2}[(\sigma_{11} - \sigma_{22})^2 + (\sigma_{22} - \sigma_{33})^2 + (\sigma_{33} - \sigma_{11})^2 + 6(\sigma_{23}^2 + \sigma_{13}^2 + \sigma_{12}^2)]}, \quad \text{(Eq. S6)}$$

where σ_{ij} $(i, j = 1,2,3)$ are the six independent components of a symmetric second-order stress tensor σ,

$$\sigma = [\sigma_{11}\ \sigma_{12}\ \sigma_{13}\ \sigma_{12}\ \sigma_{22}\ \sigma_{23}\ \sigma_{13}\ \sigma_{23}\ \sigma_{33}\ ]. \quad \text{(Eq. S7)}$$

The yield surface of von Mises model can be described by

$$F_v = \underline{\sigma} - \underline{\sigma_Y} = 0. \quad \text{(Eq. S8)}$$

When $F_v < 0$, there is only elastic deformation; when $F_v = 0$, materials start to yield and accumulate plastic strain ε^p. Given the fact that the yield stress of most metal materials will increase as accumulating plastic strain, which is referred to as the strain-hardening behavior, $\underline{\sigma_Y}$ is assumed to evolve with the equivalent plastic strain $\underline{\varepsilon}^p$. The Voce hardening law (Eq. S5) is used to characterize the low strain-hardening rate of lithium metal. The equivalent plastic strain $\underline{\varepsilon}^p$ is defined as

$$\underline{\varepsilon_p} = \sqrt{\left[\left(\varepsilon_{11}^p - \varepsilon_{22}^p\right)^2 + \left(\varepsilon_{22}^p - \varepsilon_{33}^p\right)^2 + \left(\varepsilon_{33}^p - \varepsilon_{11}^p\right)^2 + 6\left(\varepsilon_{23}^p\right)^2 + 6\left(\varepsilon_{13}^p\right)^2 + 6\left(\varepsilon_{12}^p\right)^2\right]}, \quad \text{(Eq. S9)}$$

where ε_{ij}^p are the components of the plastic strain tensor ε^p. The material constants can be calibrated by uniaxial tension tests, where σ_{11} is the only none-zero stress component and only diagonal strain components are non-zero ($\varepsilon_{22}^p = \varepsilon_{33}^p = -0.5\varepsilon_{11}^p$). Substituting the uniaxial stress and strain components in Eq. S6 and Eq. S9, we get the hardening curve $\underline{\sigma_Y}\left(\underline{\varepsilon}^p\right) = \sigma_{11}\left(\varepsilon_{11}^p\right)$ and the material constraints can be determined by fitting $\underline{\sigma_Y}\left(\underline{\varepsilon}^p\right)$ with Eq S5. Calibration results in ref[2] are adopted for this study. For the PTFE tube, a linear plastic hardening behavior is assumed, $\underline{\sigma_Y} = \sigma_0 + H\underline{\varepsilon_p}$, where σ_0 is the initial yield stress and H is the linear hardening rate. They are determined with the information provided by the supplier.

Drucker-Prager/Cap (DPC) model

DPC model consists of two yield surfaces. The former one describes the inter-granular sliding and is governed by the Drucker-Prager model,

$$F_s = q - p\ tan\ tan\ \beta\ - c = 0, \quad \text{(Eq. S10)}$$

where β is the friction angle and c is the cohesion strength. p and q are the hydrostatic pressure and equivalent stress, defined as

$$p = -\frac{1}{3}(\sigma_{11} + \sigma_{22} + \sigma_{33}), \quad \text{(Eq. S11)}$$

$$q = \underline{\sigma}. \quad \text{(Eq. S12)}$$

The other yield surface describes the intra-granular consolidation,

$$F_c = \sqrt{(p - p_a)^2 + (Rq)^2} - R(c + p_a\ tan\ tan\ \beta\ ) = 0, \quad \text{(Eq. S13)}$$

where R is the eccentricity of the ellipse, and p_a is the pressure at the intersection point of the sliding surface and the cap. Since the strength of granular media increases as being densified, the position of the consolidation yield surface (p_a) is assumed to increase with the volumetric plastic strain. The DPC plasticity model can be fully calibrated with at least three different tests, i.e., uniaxial compression, Brazilian test (lateral compression), and confined compression. Interested readers can refer to ref[4] for more details of calibration.

we simulated all the three steps that undergo mechanical loading, including 1) the SE manufacturing (compressing SE under 300 MPa pressure), 2) pre-compression (compressing the assembly with 10MPa pressure), and 3) charge process (expansion due to lithium plating).

Step 1. The initial thickness of the SE is estimated by assuming an initial relative density of 30%, which is around 3.3mm. Given that the pressure was manually applied and might deviate from the desire pressure (300 MPa), instead of applying the pressure directly, we prescribed the displacement of the upper stainless-steel bar and compressed the SE to a thickness of 0.84mm as measured from the CT image. The deformed configuration matches well with the experimental

observation. In addition, the pressure developed inside the cell is around 220 MPa. This is quite reasonable considering that the material inputs were estimated from the limited data in literature.

Step 2. The deformed SE from previous step was imported and assembled with the lithium metal and anode. Similarly, we prescribed the displacement of the upper stainless-steel bar and compressed the cell assembly gradually until the edge of lithium metal deformed around 300 μm, as measured in **Fig. 3**. The pressure developed inside the cell (8MPa) is comparable to what we applied in experiment (~10Mpa).

Step 3. We simulated the lithium plating process by introducing through-thickness thermal expansion of lithium metal. The thermal expansion coefficient is correlated to the lithium plating rate through a single-ion conduction model, a detailed description of which is given in the following. It is estimated that around 5 μm thick lithium was plated in the experiment. Therefore, we simulated the expansion up to 5 μm. Both the upper and lower stainless-steel bars were fixed during this process. As a result, the lithium further deformed and flowed deeper into the gap.

Single-ion conduction model for all-solid-state batteries

A single-ion conduction model for all-solid-state batteries was used to capture the electrochemical response[5] (**Fig. S17**). In this model, a uniform Li-ion concentration across the solid electrolyte is assumed considering that Li-ion is the only charge carrier in the electrolyte and that electroneutrality holds true throughout the layer. Reaction is assumed to occur only at the interfaces and the electrodes are non-porous. The governing equations are summarized in Table S4, and the variables and physical constants in the model are listed in Table S5 and Table S6.

Lithium plating rate R_p (thickness change per unit time) is related to $i_{c/e}$ by,

$$R_p = \frac{M_{\mathrm{Li}}}{\rho_{\mathrm{Li}} F} i_{c/e}, \qquad \text{(Eq. S14)}$$

where M_{Li} and ρ_{Li} are the molar mass and density of Lithium. We simulate this thickness change with thermal expansion by prescribing a linearly increasing temperature field with respect to time ($T = kt$). The equivalent thermal expansion coefficient is then determined by,

$$\alpha_L = \frac{R}{kL_a} = \frac{M_{\mathrm{Li}}}{k\rho_{\mathrm{Li}} F L_a} i_{c/e}. \qquad \text{(Eq. S15)}$$

Note that the current density at any cross section of the cell equals to the applied current at any time. Therefore, under constant charge and discharge the expansion coefficient will be constant. Under other loading conditions, e.g., constant voltage, the expansion coefficient will vary depending on the current flow. In this work, we only consider the constant current charge. A simulation was performed to predict the cell potential and lithium-ion concentrations. The values of the physical constants used in the simulation are listed in Table S6. The 1D single-ion conduction model can capture the cell potential before the onset of soft circuit (**Fig. S18a**), as well as the trend of lithium concentration in solid electrolyte and cathode (**Fig. S18b**).

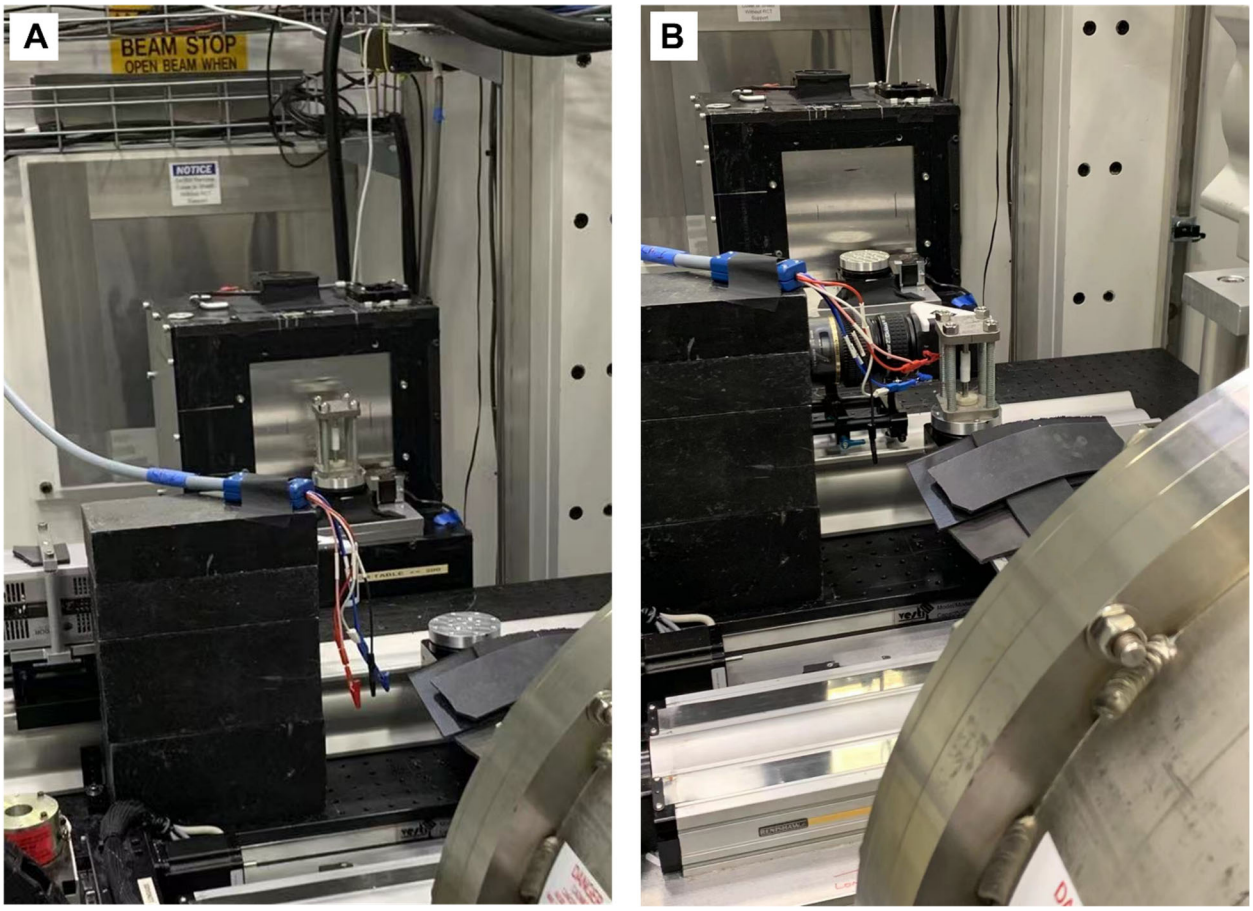

Fig. S1. Photos of the neutron imaging set up in (a) 3D neutron tomography and (b) 2D operando neutron radiography.

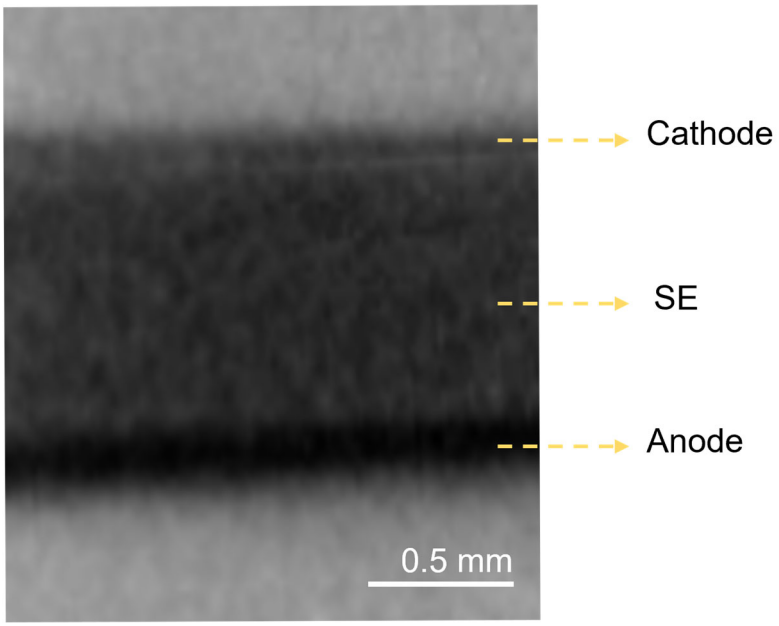

Fig. S2. Magnified 2D neutron radiograph image of the ASLMBs in the operando neutron imaging test.

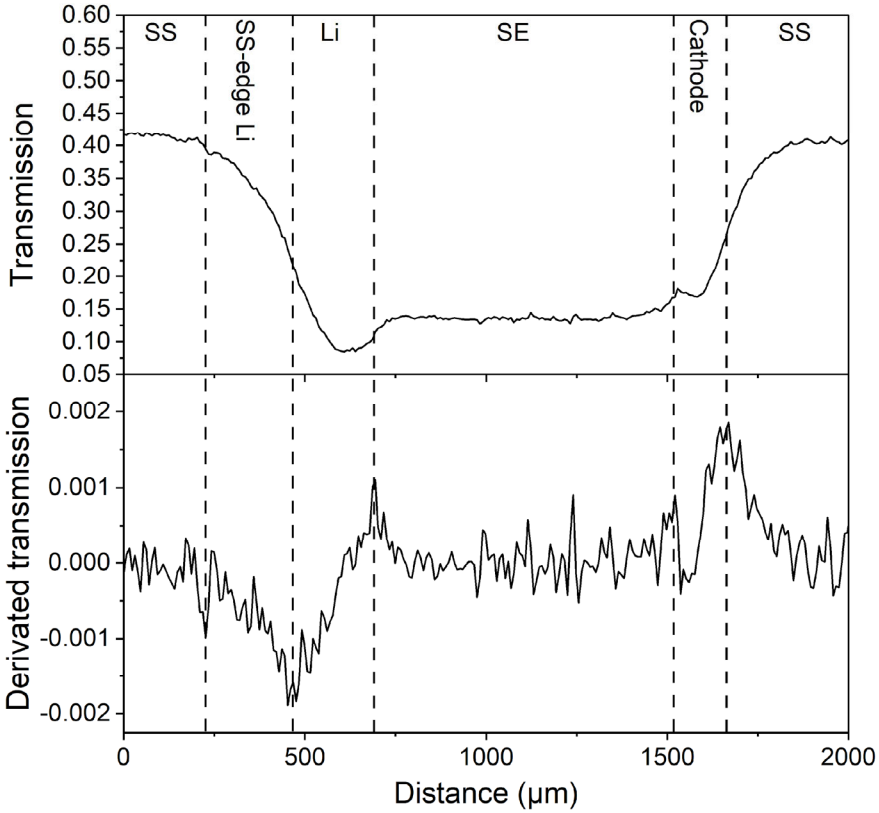

Fig. S3. Neutron transmission and derivative transmission to determine the interfaces between adjacent layers.

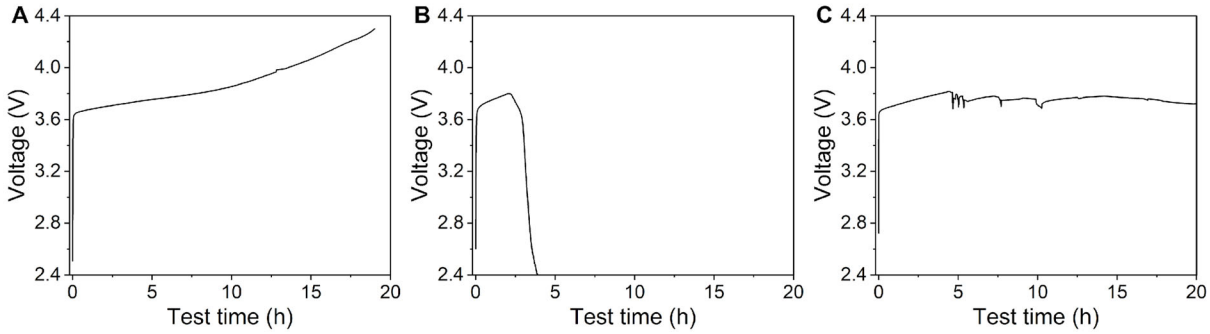

Fig. S4. Galvanostatic charge profiles of the ASLMB with (a) normal cycle, (b) hard short, and (c) soft short.

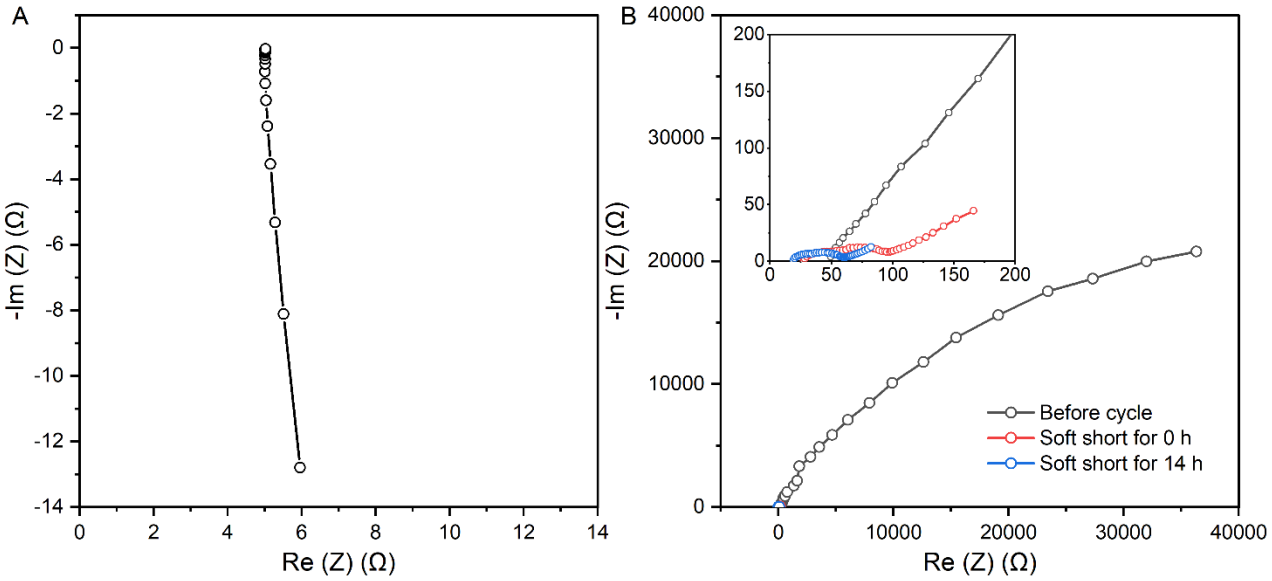

Fig. S5. Nyquist plots of the ASLMB after (A) “hard short” and (B) “soft short”.

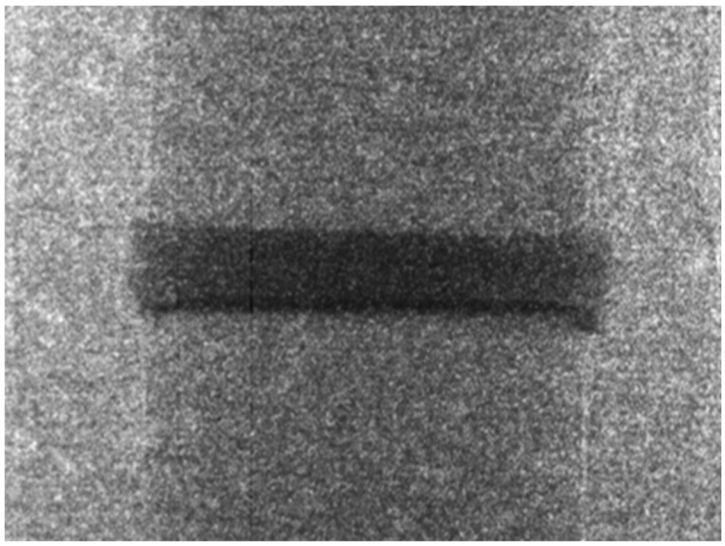

Fig. S6. Neutron radiograph image of the ASLMB without normalization treatment.

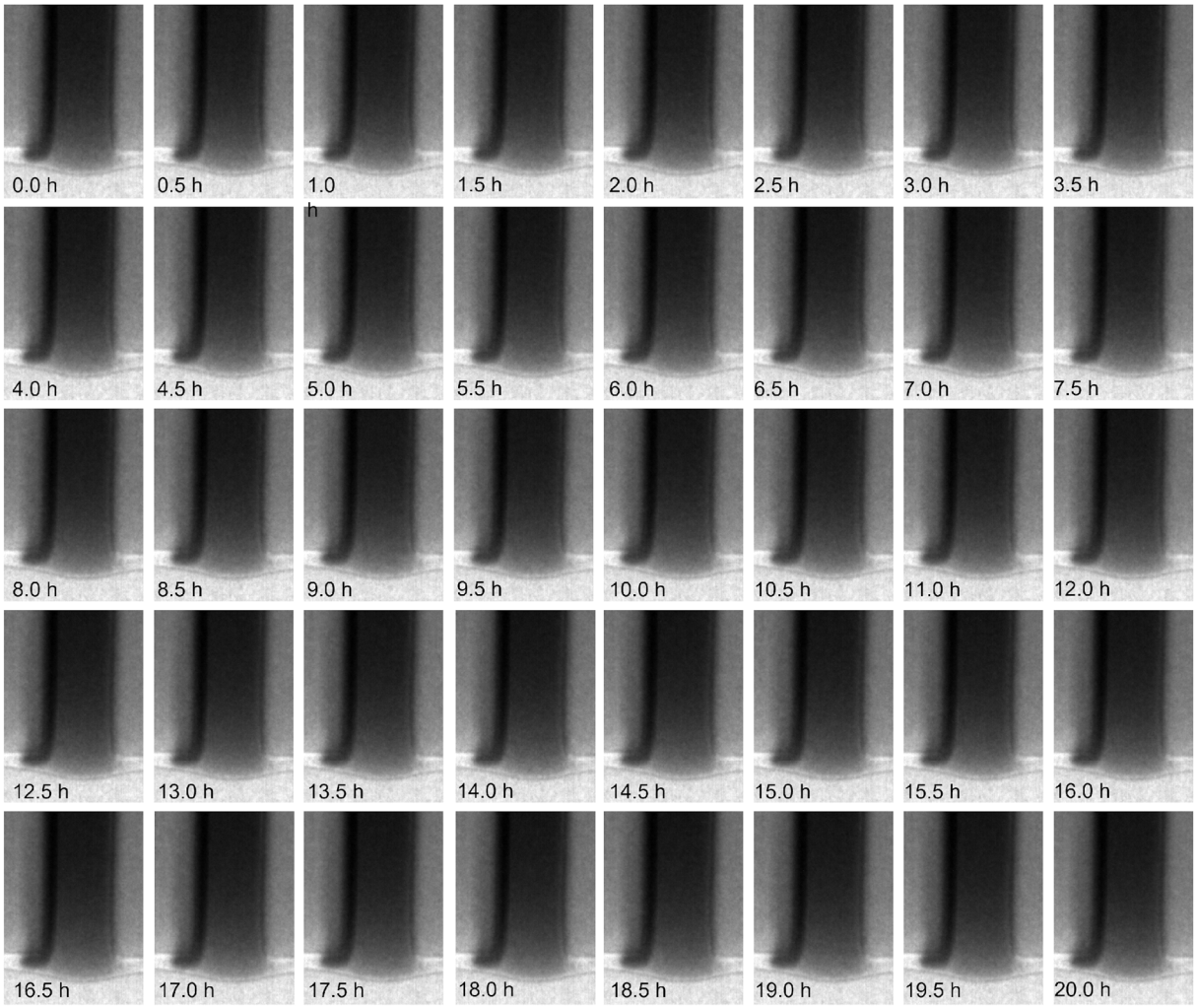

Fig. S7. Time stamped neutron radiography images during the battery test.

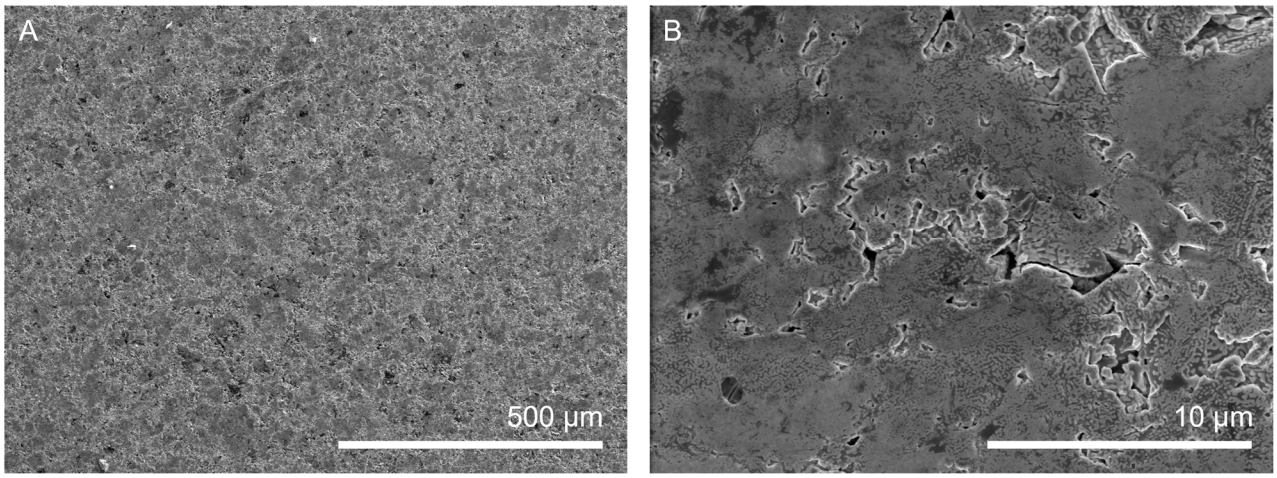

Fig. S8. SEM images of the SE pellet in the top view at (A) low and (B) high resolution.

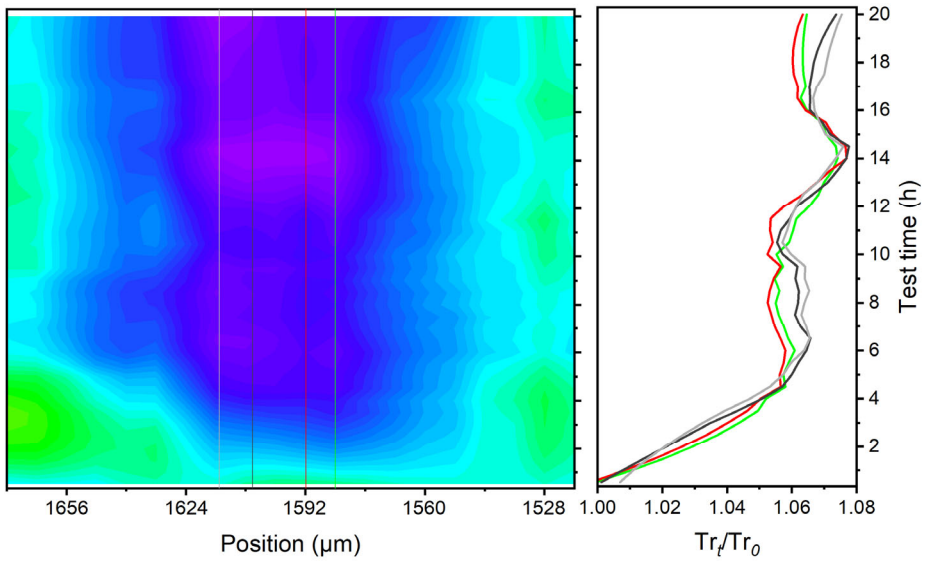

Fig. S9. The magnified intensity mapping of the real-time transmission changes at the cathode side. The real-time Trt/Tr0 evolutions at four representative positions were plotted.

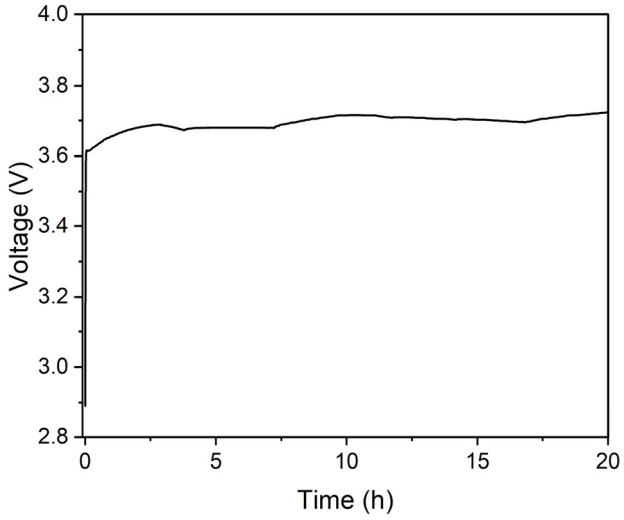

Fig. S10. Galvanostatic charge profile of the cell for XCT test.

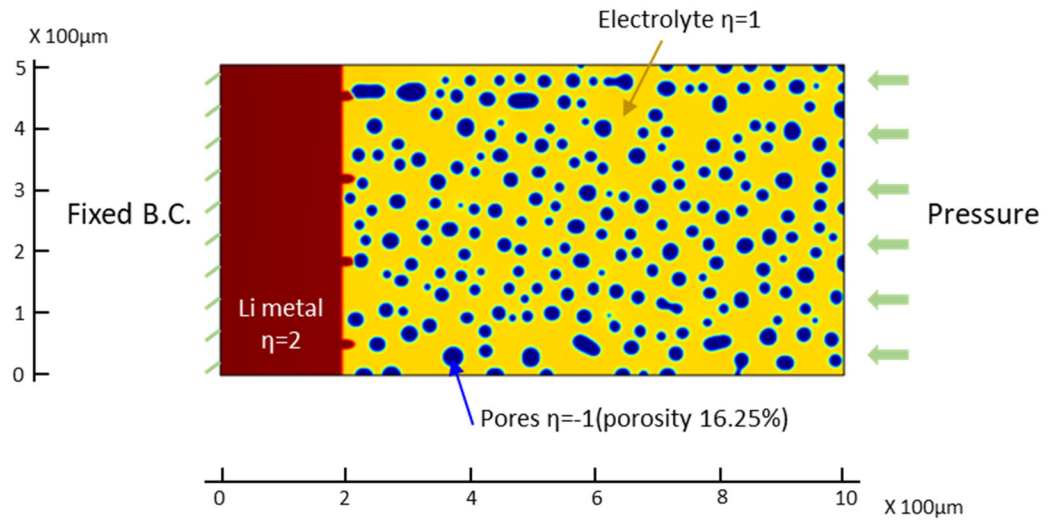

Fig. S11 Schematic diagram of boundary conditions, initial state of the system. The blue color represents the air pores phase (porosity around 16.25%)

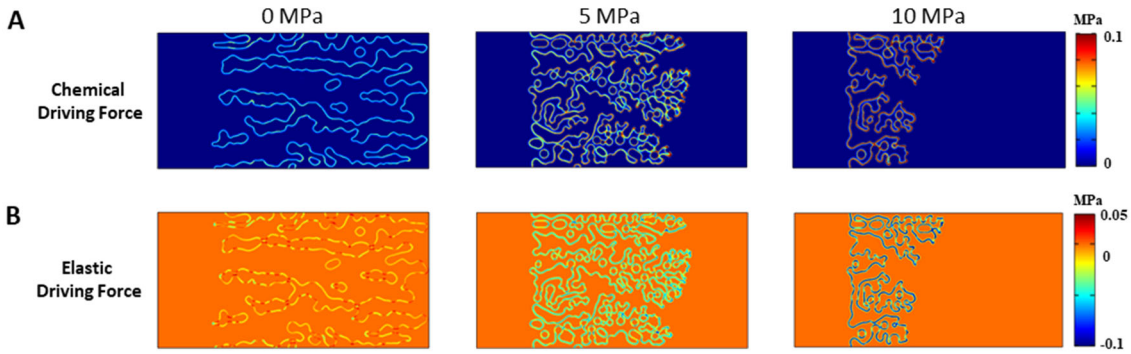

Fig. S12 Phase-field simulation results of Li dendrite growth in a porous electrolyte under external pressure of 0, 5, and 10 MPa after 500 s of evolution. (A) the chemical driving force including chemical bulk energy and electrochemical energy. (B) the elastic driving force at the electrode-electrolyte interface.

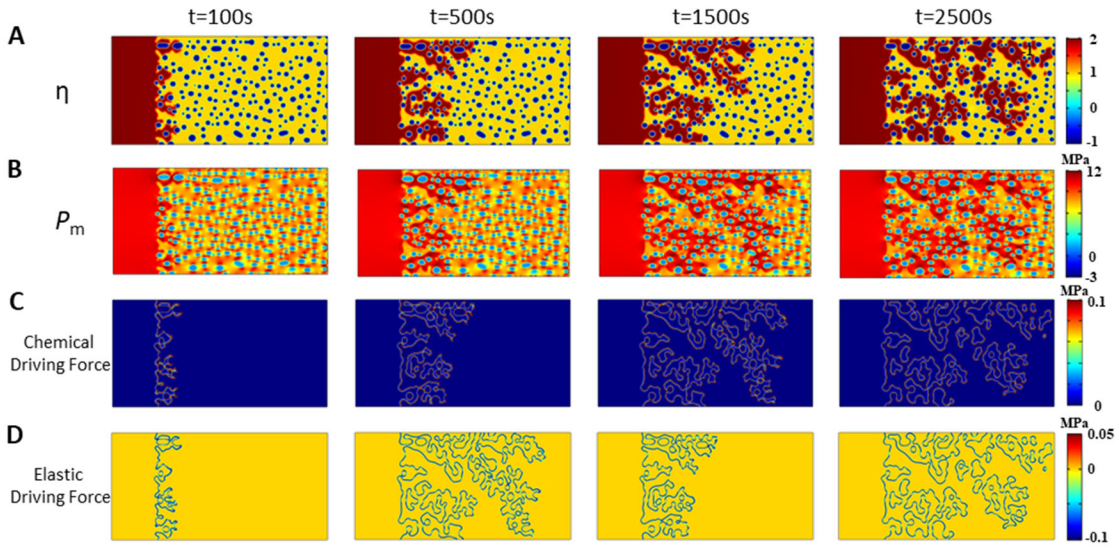

Fig. S13 Phase-field simulation results of the evolution of Li dendrite structure in a porous electrolyte under external pressure of 10 MPa. (A) dendrite morphology represented by η, where 2 corresponds to Li metal, 1 to electrolyte, 0 to Li metal filling inside the pore, -1 to pores. (B) hydrostatic pressure Pm. (C) the chemical driving force including chemical bulk energy and electrochemical energy. (D) the elastic driving force at the electrode-electrolyte interface.

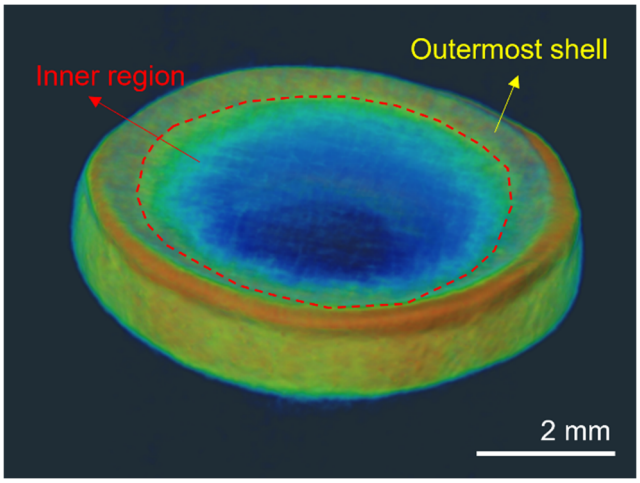

Fig. S14. Neutron CT of the ASLMB. The inner region information was lost due to the neutron absorption from the stainless steel.

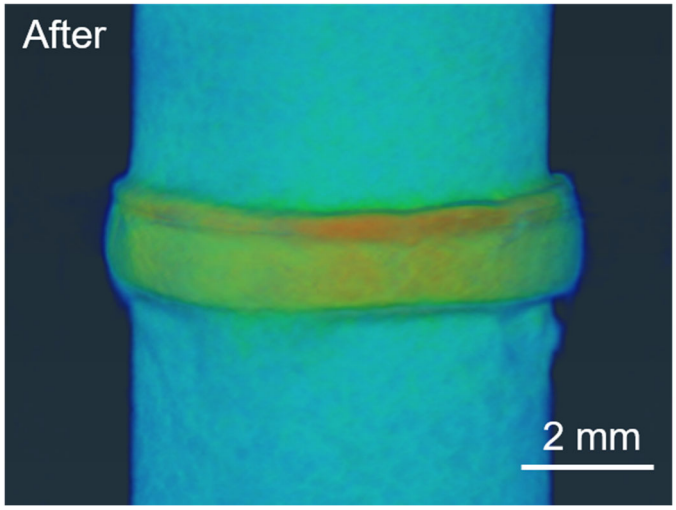

Fig. S15. Neutron CT of the ASLMB after the electrochemical test.

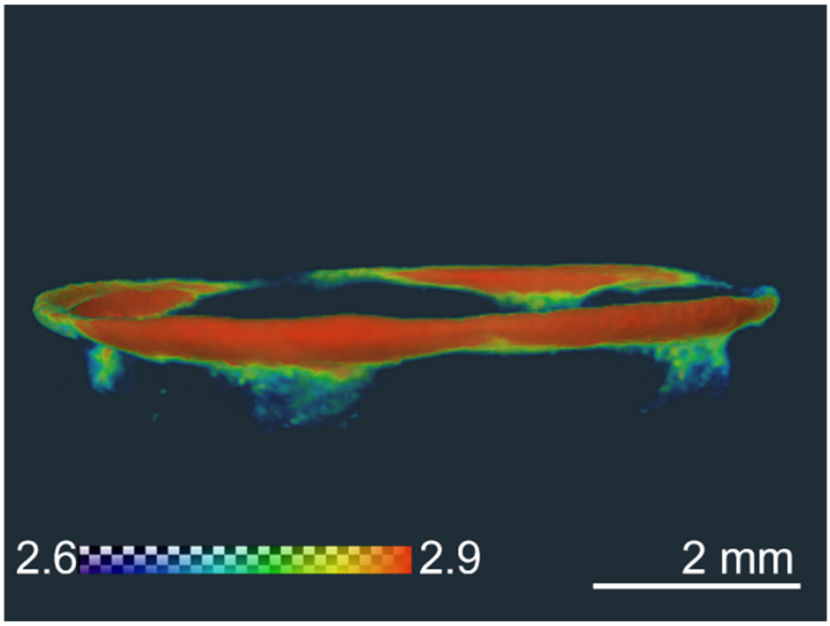

Fig. S16. Neutron CT image of the extracted Li metal.

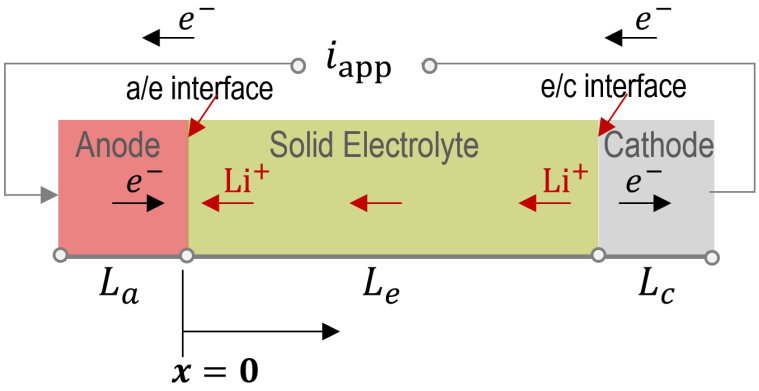

Fig. S17. Illustration of single-ion conduction model for solid-state batteries

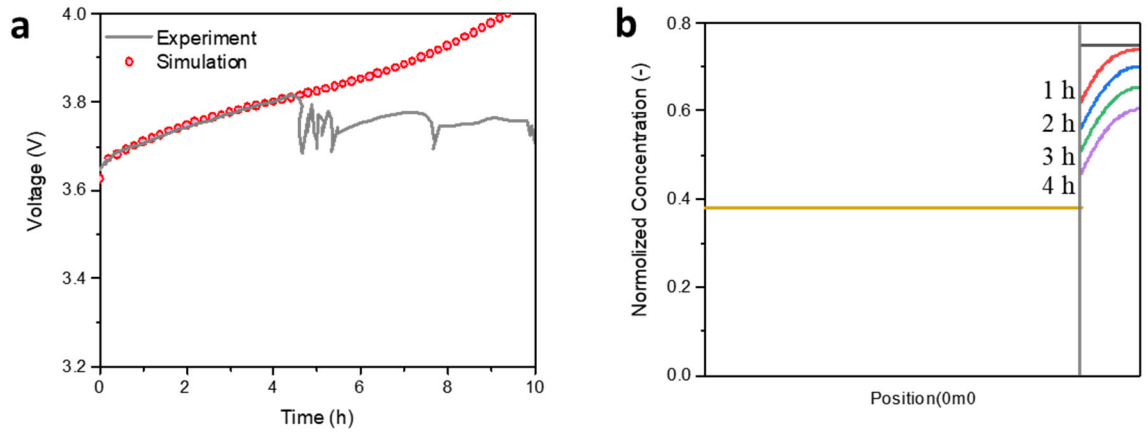

Fig. S18. Simulation results of the single-ion conduction model. (a) Cell potential, (b) Lithium concentration

Table. S1 Elemental neutron cross sections. 1fm=10^{-15} m, 1barn=10^{-24} cm^2.[6]

Elements	Li	Ni	Mn	Co	P	S	Cl	C
Neutron total cross sections	71.87	22.99	15.45	42.78	3.484	1.556	50.3	5.5545
Neutron scattering cross sections	1.37	18.5	2.15	5.6	3.312	1.026	16.8	5.551
Neutron absorption cross sections	70.5	4.49	13.3	37.18	0.172	0.53	33.5	0.0035
Neutron coherent cross sections	0.454	13.3	1.75	0.779	3.307	1.0186	11.5257	5.551
Neutron incoherent cross sections	0.92	5.2	0.4	4.8	0.005	0.007	5.3	0.001

Table. S2 Parameters in mechanical-electrochemical phase-field model[3]

Parameters	Symbols	Real Values	Symbols	Normalized Values
Interfacial mobility	L_ξ	2.22×10^{-6} m^3/(J×s)	$\tilde{L}_\xi = L_\xi \times (E_0 \times \Delta t_0)$	3333
Reaction constant	L_η	9×10^{-4} /s	$\tilde{L}_\eta = L_\eta \times \Delta t_0$	0.9
Gradient energy coefficient.	κ_0	1.0×10^{-4} J/m	$\tilde{\kappa}_0 = \kappa_0 / (E_0 \times l_0^2)$	0.01
Li^+ diffusivity in the electrode	D^m	1×10^{-14} m^2/s	$\tilde{D}^m = D^m / (l_0^2 / \Delta t_0)$	10^{-3}
Li^+ diffusivity in the electrolyte	D^e_{bulk}	1×10^{-11} m^2/s	$\tilde{D}^e = D^e / (l_0^2 / \Delta t_0)$	1.0
Li^+ diffusivity in the pore surface	D^ρ_{surf}	1×10^{-7} m^2/s		10^4
Li^+ diffusivity inside the pore	D^ρ_{in}	0 m^2/s		0
Electric conductivity in the electrode	σ^m	1.17×10^7 S/m	$\tilde{\sigma}^m = \sigma^m / (\frac{l_0^2}{\Delta t_0} \bullet \frac{c_0 F^2}{RT})$	3×10^8
Electric conductivity in the electrolyte	σ^e	0.78 S/m	$\tilde{\sigma}^e = \sigma^e / (\frac{l_0^2}{\Delta t_0} \bullet \frac{c_0 F^2}{RT})$	20
Elastic modulus of the electrode	E^m	5 GPa	$\tilde{E}^m = E^m / E_0$	3200
Elastic modulus of the electrolyte	E^e_{bulk}	5 GPa	$\tilde{E}^e_{bulk} = E^e_{bulk} / E_0$	3200
Elastic modulus of the pores	E^ρ	1×10^{-4} GPa	$\tilde{E}^p = E^p / E_0$	0.07
Poisson's ratio	v	0.36		0.36
Eigenstrain coefficients	V_{11}	0.866×10^{-3}		0.866×10^{-3}
	V_{22}	0.773×10^{-3}		0.773×10^{-3}
	V_{33}	0.529×10^{-3}		0.773×10^{-3}
Charge transfer coefficients	α, β	0.5		0.5
Accumulation constant	K	1.8 mol/L	$\tilde{K} = K / c_0$	1.8
Current constant	R	1.2×10^3 J/m^3	$\tilde{R} = R / E_0$	0.0008
Spatially mobility	$M(\rho)$			1.56×10^{-4}
Gradient energy coefficient	κ_ρ			1.56×10^{-4}

Table. S3 Material constants of each component used in the FEM simulations

Materials	**Material models and constants**					
	Elasticity		Drucker-Prager/Cap			
	E(GPa)	v (-)	β (°)	c (MPa)	R (-)	p_a (MPa)
Cathode	5.0	0.1	65	1.0	0.8	**Fig. 4E**
SE	5.0	0.1	65	4.0	0.8	**Fig. 4E**
	Elasticity		Plastic Hardening			
	E(GPa)	v (-)	σ_0 (MPa)	σ_s (MPa)	β (-)	
Lithium metal	7.8	0.33	1.024	1.389	22.27	
			σ_0 (MPa)	H (MPa)		
PTFE tube	0.42	0.33	20.0	133.3		
Stainless steel	21.0	0.33				

Table. S4 Governing equations and boundary conditions of the single-ion conduction model

	Equation	Boundary Condition
Charge Transfer, Solid Electrolyte	$i_e = -\kappa_e \frac{\partial \phi_e}{\partial x}$	$i_e(x = 0) = i_{a/e}$, $i_e(x = L_e) = -i_{e/c}$
Charge Transfer, Cathode	$i_c = -\sigma_c \frac{\partial \phi_c}{\partial x}$	$i_c(x = L_e) = -i_{e/c}$, $i_e(x = L_e + L_c) = i_{\text{app}}$
Mass Transport, Cathode	$\frac{\partial c}{\partial x} = \frac{\partial}{\partial x}\left(D_c \frac{\partial c}{\partial x}\right)$	$\frac{\partial \text{c}}{\partial x}(x = L_e) = -\frac{i_{e/c}}{FD_c}$, $\frac{\partial \text{c}}{\partial x}(x = L_e + L_c) = 0$
Reaction Kinetics, Interfaces	$i_s = i_s^0 \left[\exp\left(\frac{\alpha F}{RT}\eta\right) - \exp\left(-\frac{(1-\alpha)F}{RT}\eta\right)\right], s = a/e, e/c$	
	$i_{a/e}^0 = Fk_a,\ i_{e/c}^0 = Fk_c(c_{\max} - c)^\alpha c^{1-\alpha}$	

Table. S5 Variables in the single-ion conduction model

Variable	Physical meaning
i_e, i_c	Current density in electrolyte and cathode
ϕ_e, ϕ_c	Potential field in electrolyte and cathode
c	Lithium-ion concentration in cathode
η	Over-potential at interfaces, $\eta = [\phi] - U_{\mathrm{ocv}}$, where $[\phi]$ is the potential jump at electrolyte/electrode interface and U_{ocv} is the open circuit potential.

Table. S6 Physical constants and the values used in the simulation

Variable	Physical meaning	Value
L_e, L_c	Thickness of electrolyte and cathode	840 μm / 130 μm
k_e	Ion conductivity of solid electrolyte	7.8 $\mathrm{mS/cm}$
σ_c	Electron conductivity of cathode	38 $\mathrm{mS/cm}$
D_c	Ion diffusivity of cathode	8e-8 $\mathrm{cm^2/s}$
α	Anodic charge transfer number	0.5
k_a, k_c	Standard rate coefficient for anode/electrolyte and electrolyte/cathode interfaces	4.56e-9 $\mathrm{mol/(cm^2 \cdot s)}$
i_{app}	Applied current density	0.4 $\mathrm{mA/cm^2}$

References

[1] a) Y. Ren, Y. Zhou, Y. Cao, *The Journal of Physical Chemistry C* **2020**, 124, 12195; b) Y. Ren, K. Zhang, Y. Zhou, Y. Cao, *ACS Applied Materials & Interfaces* **2022**, 14, 30658.

[2] J. Zhu, T. Wierzbicki, W. Li, *J. Power Sources* **2018**, 378, 153.

[3] T. Sedlatschek, J. Lian, W. Li, M. Jiang, T. Wierzbicki, M. Z. Bazant, J. Zhu, *Acta Mater.* **2021**, 208, 116730.

[4] J. Zhu, W. Li, T. Wierzbicki, Y. Xia, J. Harding, *Int. J. Plast.* **2019**, 121, 293.

[5] S. D. Fabre, D. Guy-Bouyssou, P. Bouillon, F. Le Cras, C. Delacourt, *J. Electrochem. Soc.* **2011**, 159, A104.

[6] V. F. Sears, *Neutron News* **1992**, 3, 26.